Received: 18 October 2018 | Revised: 30 January 2019 | Accepted: 5 February 2019

DOI: 10.1111/bre.12345

ORIGINAL ARTICLE

WILEY Basin Research IAS EAGE

Spatial distribution of micrometre-scale porosity and permeability across the damage zone of a reverse-reactivated normal fault in a tight sandstone: Insights from the Otway Basin, SE Australia

Natalie Debenham[1] | **Natalie J. C. Farrell**[2] | **Simon P. Holford**[1] | **Rosalind C. King**[3] | **David Healy**[2]

[1]Australian School of Petroleum, Centre for Tectonics, Resources and Exploration (TRaX), The University of Adelaide, Adelaide, South Australia, Australia

[2]School of Geosciences, King's College, The University of Aberdeen, Aberdeen, UK

[3]Department of Earth Sciences, Centre for Tectonics, Resources and Exploration (TRaX), The University of Adelaide, Adelaide, South Australia, Australia

Correspondence
Natalie Debenham, Australian School of Petroleum, Centre for Tectonics, Resources and Exploration (TRaX), The University of Adelaide, SA, Australia.
Email: natalie.debenham@adelaide.edu.au

Funding information
Australian Research Council, Grant/Award Number: Discovery Project DP160101158; Petroleum Exploration Society of Australia; Australian Petroleum Production and Exploration Association; Natural Environment Research Council, Grant/Award Number: NE/N003063/1; Australian Government Research Training Program Scholarship

Abstract

Knowledge of the permeability structure of fault-bearing reservoir rocks is fundamental for developing robust hydrocarbon exploration and fluid monitoring strategies. Studies often describe the permeability structure of low porosity host rocks that have experienced simple tectonic histories, while investigations of the influence of faults with multiple-slip histories on the permeability structure of porous clastic rocks are limited. We present results from an integrated petrophysical, microstructural, and mineralogical investigation of the Eumeralla Formation (a tight volcanogenic sandstone) within the hanging wall of the Castle Cove Fault which strikes 30 km NE–SW in the Otway Basin, southeast Australia. This late Jurassic to Cenozoic-age basin has experienced multiple phases of extension and compression. Core plugs and thin sections oriented relative to the fault plane were sampled from the hanging wall at distances of up to 225 m from the Castle Cove Fault plane. As the fault plane is approached, connected porosities increase by ca. 10% (17% at 225 m to 24% at 0.5 m) and permeabilities increase by two orders of magnitude (from 0.04 mD at 225 m to 1.26 mD at 0.5 m). Backscattered Scanning Electron Microscope analysis shows that microstructural changes due to faulting have enhanced the micrometre-scale permeability structure of the Eumeralla Formation. These microstructural changes have been attributed to the formation of microfractures and destruction of original pore-lining chlorite morphology as a result of fault deformation. Complex deformation, that is, formation of macrofractures, variably oriented microfractures, and a hanging wall anticline, associated with normal faulting and subsequent reverse faulting, has significantly influenced the off-fault fluid flow properties of the protolith. However, despite enhancement of the host rock permeability structure, the Eumeralla Formation at Castle Cove is still considered a tight sandstone. Our study shows that high-resolution integrated analyses of the host rock are critical for describing the micrometre-scale permeability structure of reservoir rocks with high

porosities, low permeabilities, and abundant clays that have experienced complex deformation.

KEYWORDS

Otway Basin, permeability, porosity, reverse-reactivated normal fault

Highlights

- Porosity and permeability increase toward the Castle Cove Fault
- Enhanced connectivity toward the fault is related to an increase in microfractures
- Destruction of chlorite morphology also contributes to enhanced connectivity
- Macrofracture network at Castle Cove would be the most effective fluid flow conduit

1 | INTRODUCTION

Fault zones and their related fracture patterns control fluid flow within the Earth's brittle upper crust at a range of scales (Caine, Evans, & Forster, 1996). Knowledge of the permeability structure of brittle fault zones is critical for predicting hydrocarbon migration, accumulation, and leakage in sedimentary basins (Aydin, 2000; Knipe, Jones, & Fisher, 1998), fluid migration in geothermal plays and hydrothermal ore deposits (Fairley, 2009; Rowland & Sibson, 2004; Sibson, Moore, & Rankin, 1975), fluid migration in water aquifers (Bense & Person, 2006; Folch & Mas-Pla, 2008), and for identifying potential sites for deep-waste storage repositories for the disposal of CO_2 and radioactive waste (Bredehoeft, 1997; Streit & Hillis, 2004). In recent years, there has been considerable work on the structure, mechanics, and fluid flow properties of fault zones and their associated permeability structures (Bense, Gleeson, Loveless, Bour, & Scibek, 2013; Faulkner et al., 2010). However, challenges associated with predicting fluid flow in the sub-surface arise due to the complex nature of fault zones and the variable impact deformation induced features have on fluid flow.

Deformation associated with faulting can either enhance or impede the permeability of fault-bearing rocks (Caine et al., 1996; Faulkner et al., 2010; Fisher & Knipe, 1998). Within a fault damage zone, macrofractures and dilational deformation bands will increase permeability (Bense et al., 2013; Faulkner et al., 2010; Fossen, Schultz, Shipton, & Mair, 2007). Fluid flow within these deformation-related permeability structures occurs cyclically in a transient manner, in response to fluid pressure fluctuations associated with earthquake slip (Sibson, 1994; Woodcock, Dickson, & Tarasewicz, 2007). In contrast, compartmentalisation during faulting and the formation of compaction and shear deformation bands can impede fluid flow within a fault damage zone (Bense et al., 2013; Fossen et al., 2007). While outcrop-scale structures can be accounted for during conventional reservoir modelling of fault zone permeability structure, micrometre-scale heterogeneities are often overlooked.

At the micrometre-scale, the petrophysical properties of a host rock can also be significantly altered as a result of faulting-related deformation. For instance, the magnitude of permeability can be degraded due to pore collapse, grain crushing, and cement precipitation during deformation (Bense et al., 2013; Farrell & Healy, 2017; Fisher & Knipe, 1998). Alternatively, the magnitude of permeability can be enhanced through the formation of grain-scale microfractures (Anders, Laubach, & Scholz, 2014) and changes in grain morphology through dilation and disaggregation (Bense et al., 2013). As effective pressure increases (i.e. increasing depth in the crust), it is predicted that microfractures will exert a greater influence on permeability than macrofractures (Nara, Meredith, Yoneda, & Kaneko, 2011). Therefore, understanding how rocks deform at the micrometre-scale is fundamental for defining off-fault fluid flow properties of reservoir rocks in sedimentary basins.

A large number of previous studies have focussed on the permeability structure of faulted porous rocks in outcrops which have experienced simple tectonic histories (i.e. faults with a single-slip history; e.g. Antonellini & Aydin, 1994; Bauer, Meier, & Philipp, 2015; Farrell, Healy, & Taylor, 2014; Shipton, Evans, Robeson, Forster, & Snelgrove, 2002); however, few studies have investigated the influence of complex faults (i.e. faults with a multiple-slip history) on the micrometre-scale permeability structure of porous clastic rocks in sedimentary basins. Motivated by this, we aim to understand the influence of inverted faults with multiple-slip histories on the micrometre-scale permeability structure of sandstones. We focus on an inverted fault that was initiated as a normal fault and was subsequently reactivated as a reverse fault. We identify the faulting-related deformation processes that control the permeability structure of the protolith within the hanging wall of the fault. Furthermore, we describe the influence of this deformation on fluid flow adjacent to the fault and the implications this has on diagenesis.

To address the aims of this study, we describe the relationships between the petrophysical, microstructural, and mineralogical properties of a porous sandstone with low permeabilities (i.e. a tight sandstone) within the damage zone of a reverse-reactivated fault, the Castle Cove Fault in the Otway Basin, southeast Australia. This study area provides an excellent opportunity to address the influence of a reverse-reactivated normal fault on the micrometre-scale permeability structure of porous sandstones. High-resolution analyses have been undertaken on core-plugs and thin sections oriented relative to the fault plane, at distances of up to 225 m from the Castle Cove Fault. We show that connected porosity, permeability, and pore connectivity increase as the fault plane is approached (from 225 to 0.5 m from the fault plane), where fracturing occurs at a range of scales and pore-lining clays become disaggregated as a result of fault-related deformation. Enhancement of the micrometre-scale permeability structure is attributed to these faulting-induced microstructural and clay morphology changes within the hanging wall.

2 | GEOLOGICAL BACKGROUND

The Otway Basin is a late Jurassic to Cenozoic sedimentary basin located on the south-eastern margin of Australia (Figure 1). The basin formed following Tithonian rifting and continental breakup of Australia and Antarctica (Norvick & Smith, 2001), and has since experienced a complex tectonic history with multiple phases of extension and compression (Debenham, King, & Holford, 2018; Holford et al., 2014; Krassay, Cathro, & Ryan, 2004; Perincek, Simons, & Pettifer, 1994; Schneider, Hill, & Hoffman, 2004; Tassone, Holford, Hillis, & Tuitt, 2012; Tassone, Holford, King, Tingay, & Hillis, 2017). In the eastern Otway Basin, a series of NE–SW striking faults intersect the coastline (Figure 1). Many of these faults are well-exposed within the youngest unit of the Aptian to Albian Eumeralla Formation. The Eumeralla Formation is a fine- to medium-grained, compositionally immature volcanogenic sandstone with thin coal seams. The Eumeralla Formation was deposited in a high-energy, fluvial environment with braided channels, flood plains, and shallow lacustrine deposits (Krassay et al., 2004). Contemporaneous volcanism to the east of the basin formed the main source of volcanogenic clastics to the Eumeralla Formation (Duddy, 2003). The formation is lithologically variable and is characterised by different diagenetic zones of alteration (Duddy, 2002, 2003). Pervasive diagenesis within the Eumeralla Formation has resulted in the significant destruction of porosity and permeability under moderate burial depths of <1,500 m (Tassone, Holford, Duddy, Green, & Hillis, 2014). Intraformational seals and interbedded coal seams within the lower section of the formation are the source of hydrocarbon

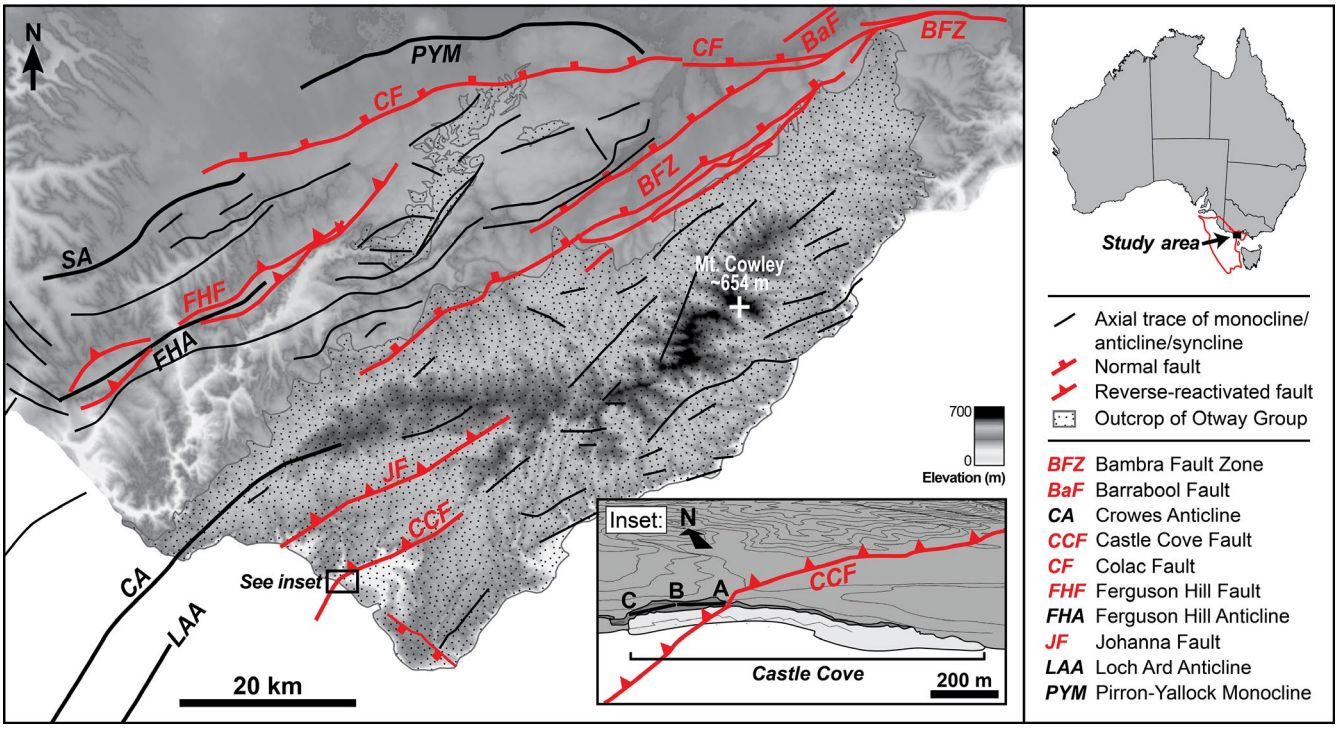

FIGURE 1 A structural map showing neotectonic structural discontinuities in the eastern Otway Basin, modified after Debenham et al. (2018). The map is underlain by a digital elevation model from Geoscience Australia. Note that the elevation scale only applies to the structural map. The inset illustrates the location of Castle Cove and the strike of the Castle Cove Fault. The locations of the A–B and B–C cross sections are also shown (Figure 2)

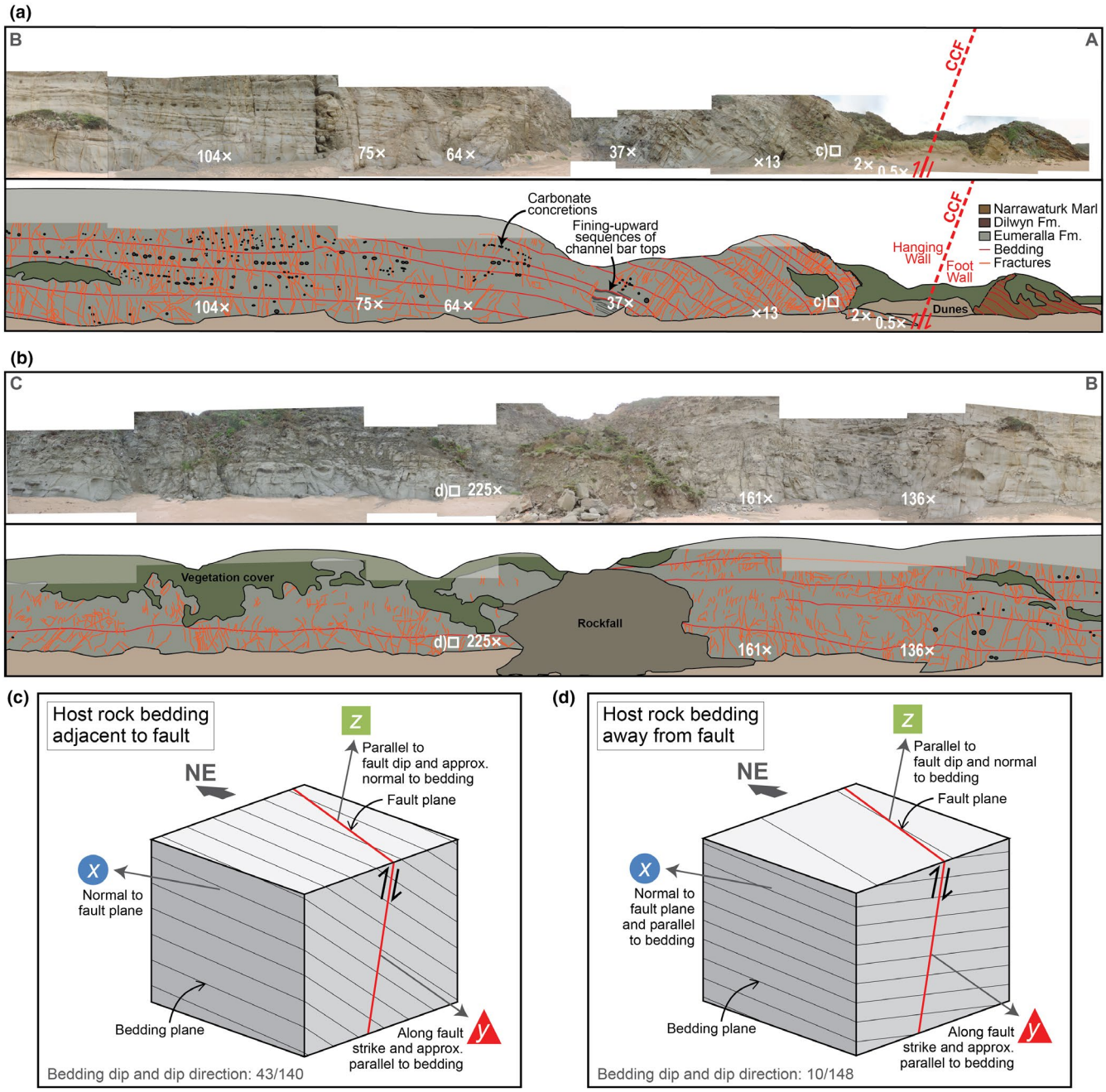

FIGURE 2 Photo and schematic diagram of the study site at Castle Cove in the Otway Basin, southeast Australia, after Debenham et al. (2018). (a) Photo and schematic diagram of A–B cross-section (Figure 1) of the cliff exposures at Castle Cove. Sample locations are indicated by white crosses. Red lines indicate bedding planes and orange lines indicate macrofractures visible in the photos. (b) Photo and schematic diagram of B–C cross-section (Figure 1). (c) Example of the host rock bedding orientation at distance from the Castle Cove Fault, and (d) example of the host rock bedding orientation adjacent to the fault

accumulations discovered within the eastern Otway Basin (Boreham et al., 2004; Edwards, Struckmeyer, Bradshaw, & Skinner, 1999), and therefore this is an important interval for petroleum exploration.

This study is focussed on a well-exposed damage zone of the seismic-scale Castle Cove Fault, located in the eastern Otway Basin, Australia (Figures 1 and 2). The Castle Cove Fault is a NE–SW striking, reverse-reactivated normal fault with a strike length of ca. 30 km (Debenham et al., 2018). The fault plane steeply dips to the northwest (Debenham et al., 2018). The fault was initiated as a normal fault in the late Cretaceous and reactivated as a reverse fault during the late Miocene to Pliocene (Debenham et al., 2018; Duddy, 1994; Edwards, Leonard, Pettifer, & Mcdonald, 1996; Holford et

al., 2014). Fault throw is estimated to be between 250 and 1,000 m of vertical displacement (Debenham et al., 2018).

The fault core is not exposed at the surface, but the damage zone is well-exposed and extends more than 300 m in the hanging wall to inaccessible cliff exposures (Debenham et al., 2018). Within 25 m of the fault plane, a zone of maximum macrofracture density within the fault damage zone has been identified by Debenham et al. (2018). Structural mapping also identified 11 macrofracture sets within the fault damage zone at Castle Cove, with three Andersonian shear macrofracture sets geometrically related to the Castle Cove Fault; (a) late Cretaceous normal movement of the Castle Cove Fault resulted in the formation of the first and most spatially extensive fracture set, (b) non-coaxial inversion during anticlinal folding resulted in the formation of the second fracture set, and (c) fault reverse-reactivation and anticlinal folding also resulted in the formation of the final fracture set (Debenham et al., 2018). At Castle Cove, a series of small-scale synthetic and antithetic faults, with similar and opposite geometries to the Castle Cove Fault respectively, have been identified in the hanging wall damage zone (Debenham et al., 2018).

3 | METHODS

3.1 | Samples

Ten oriented sample blocks (ca. 20 cm cubes) were collected within the hanging wall at distances between 0.5 and 225 m from the Castle Cove Fault plane (Figure 3). Sample blocks were carefully removed in a manner that preserves the natural appearance of the rock exposure. Macroscopic sedimentary features (such as channels, dewatering structures, and changes in lithology that could be observed at the outcrop-scale) were avoided during sampling as this study only focusses on micrometre-scale host rock petrophysical properties. Macrofractures, that is, fractures that are visible at the outcrop scale, and deformation bands were also avoided for this reason. Micrometre-scale features (such as laminations and bedding) could not be avoided. Sample blocks collected between 64 and 225 m were sampled from the same stratigraphic bed, however samples closer to the fault (<64 m) were collected in different stratigraphic levels as the beds were tilted up to 43° within a hanging wall anticline (>80 m in half-wavelength; Figure 2). All sample blocks were sampled from the same facies within ca. 30 m of stratigraphic height to ensure comparable host rock properties.

From the oriented sample blocks, core plugs were drilled in three orientations with respect to the fault plane, that is, normal to the fault plane (x), along fault strike (y), and parallel to fault dip (z; Figure 3). A total of 78 core plugs were drilled, which comprised of two to three repeat core plugs drilled in each orientation for each sample block. The core plugs were ca. 2.55 cm in diameter and between 2.66 and 8.12 cm in length. The dimensions of the core plugs were used to calculate bulk volume.

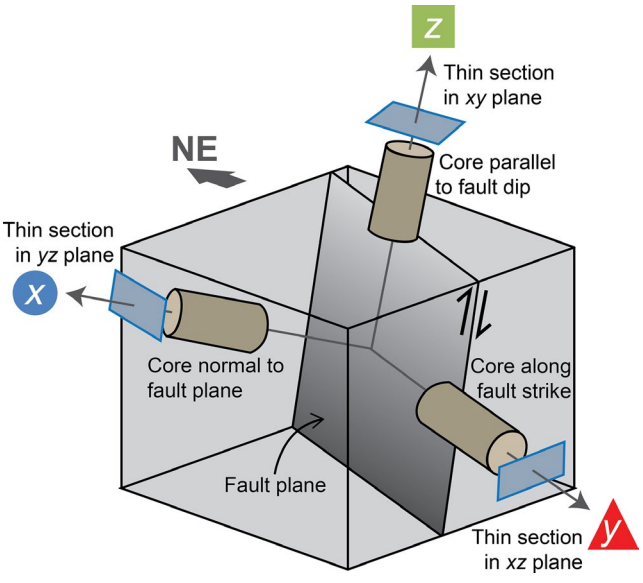

FIGURE 3 A schematic diagram of the oriented sample blocks with core plug and thin section orientations, relative to the Castle Cove Fault plane. Modified after Farrell et al. (2014)

3.2 | Porosity

A helium injection porosimeter was used to measure the connected porosity (i.e. effective porosity) of the core plugs at room temperature. Following two temperature and pressure calibration runs, helium was injected into a reference volume and stabilised at 100 psi. Next, the helium was expanded into a chamber containing the core plugs and the pressure was recorded. The equilibrium pressure of the two chambers was derived. Based on Boyle's Law of expansion, the direct grain volume of the core plugs can be calculated. To find the pore volume (v_{pore}), the grain volume (v_{grain}) was subtracted from the bulk volume of the core plugs. Porosity (φ, percentage) was calculated using Equation (1):

$$\varphi = 100 * v_{pore} / \left(v_{pore} + v_{grain}\right) \quad (1)$$

3.3 | Permeability

A nitrogen permeameter was used to measure steady state permeability of the core plugs at ambient pressures (<2.8 MPa). A meniscus flowmeter attachment was used for core plugs with low permeabilities. Permeability (k, millidarcies) was calculated using a modified Darcy equation, which is expressed by Equation (2):

$$K = 2\mu Q \left(\frac{L}{A}\right) / \left(P_1^2 - P_2^2\right) \quad (2)$$

where μ = dynamic viscosity of the gas (centipoise), Q = gas flow rate (cm^3/s), L = core plug length (cm), A = core plug cross-sectional area (cm^2), and P_1 = input gas pressure and P_2 = output gas pressure (atmospheres). Average gas pressure (P_{mean}) was calculated using a range of P_1 and P_2 values for each core plug test. To correct the permeability for gas slippage or the Klinkenberg Effect, Klinkenberg-corrected permeability was measured by plotting K against $1/P_{mean}$. The Klinkenberg-corrected permeability value was identified where the line of best fit intersected the y-axis of the plot. This value represents the permeability at which the gas is compressed by infinite pressure and acts as a liquid (Klinkenberg, 1941). If the line of best fit had a coefficient of determination (R^2) that was <0.9, the permeability was re-analysed.

3.4 | Pore throat size and connectivity

Connected pore throat size and pore connectivity were determined using a Micromeritics AutoPore IV 9500 mercury intrusion porosimeter. Mercury Injection Capillary Pressure (MICP) analyses were performed on small offcuts of the core plugs. A non-wetting phase, that is, mercury, was injected in increasing pressure increments (2–60,000 psi) into the sample blocks. The volume of mercury injected at each pressure increment was recorded. Pore throat size and size distributions were determined using a series of calculations described by Webb (2001). Mercury injection curves were used to determine the threshold injection pressure of mercury (Katz & Thompson, 1987), which is the pressure at which the mercury forms interconnected pathways between pores, that is, pore connectivity.

3.5 | Grain size

For all 10 samples, replicate analysis of grain size was undertaken on a LS13320 Laser Diffraction Particle Size Analyser following the methods of Blott, Croft, Pye, Saye, and Wilson (2004). Sub-samples from core plugs were dried and disaggregated through gentle physical disaggregation with a mortar and pestle, followed by ultrasonication with a chemical dispersant solution to reduce flocculation (Blott et al., 2004). The powdered samples were loaded into a holding tank and sonicated to reduce obscuration. The samples interact with an illuminating beam (Fourier lens) that focuses the scattered light. An array of photodetectors records the scattered light intensity patterns and calculates size distributions (volumes) of grains between 0.04 and 2000 μm.

3.6 | Thin section analysis

Thin sections were prepared in each orientation with respect to the fault plane (Figure 3) for mineralogical and microstructural analysis on a FEI Quanta 600 backscattered Scanning Electron Microscope (bSEM) with mineral liberation analysis capabilities and a Nikon Eclipse LV100 POL petrographic microscope, respectively. Mineral liberation analysis provided quantitative estimates of the mineralogical composition of the thin sections. Thin sections were injected with blue epoxy to highlight pore space and microstructures. The density of microfractures was calculated from thin sections oriented in the xz plane (Figure 3). Within each thin section, three areas (totalling 16.37 mm^2) were selected at random and the number of microfractures was counted. This yields the microfracture density in terms of the number of microfractures per squared millimetre (mm^2). The microfractures were consistently counted at 25× total magnification. Microfractures were predominately counted in quartz grains as they have less fracture anisotropy in comparison to feldspars, and is therefore considered to be a good proxy for measuring grain-scale damage (c.f. Mitchell & Faulkner, 2009). As microfractures were primarily counted in quartz grains, the number of fractures per mm^2 will be an underestimate of the total number of fractures per mm^2 within the host rock. While the density of microfractures is expected to be an underestimate, the method will identify microfracture density changes relative to distance to the fault. Microfracture type (i.e. intragranular, transgranular, and grain boundary), cement (i.e. open or sealed), and orientations were also recorded.

4 | RESULTS

4.1 | Core plug porosity

Connected porosities were measured from 78 oriented core plugs sampled from 10 sample blocks of the faulted sandstone. Overall, mean porosities increase by 10% in the hanging wall as the fault plane is approached, from 17% at distance to the fault (225 m) to 24% adjacent to the fault (0.5 m); within 0.5 m of the fault plane, high porosities of up to 27% are recorded within the hanging wall. Core plug porosities are plotted relative to distance from the fault plane (Figure 4a). Porosities are shown for three orientations (x, y, and z) relative to the fault plane. At distance from the fault plane (225 and 161 m), similar porosities are recorded. This is followed by steady increase in porosities from 161 to 75 m. There is a peak in porosities at 75–64 m which drops off to lower porosities at 37 m before increasing again toward the fault plane (Figure 4a) in the zone of maximum fracture density identified within the damage zone (Debenham et al., 2018).

4.2 | Core plug permeability

Steady state permeabilities were measured from 76 oriented core plugs. Two core plugs were too short in length and

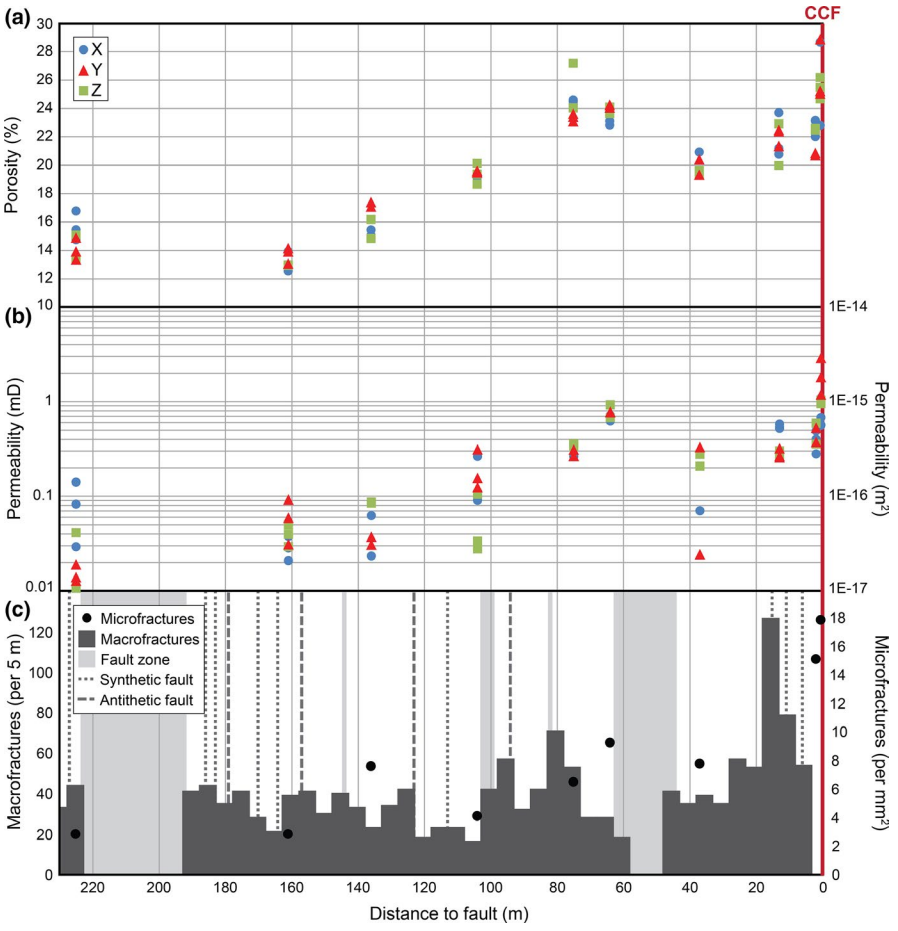

FIGURE 4 Changes in porosity, permeability, and fracture densities within the hanging wall relative to distance to the Castle Cove Fault (CCF). The *x*-axis has been reversed to represent the configuration of the outcrop, that is, 230 m is northwest and 0 m is southeast. (a) Core plug porosities from three orientations (*x*, *y*, and *z*) relative to the Castle Cove Fault plane. (b) Klinkenberg-corrected, core plug permeabilities from three orientations (*x*, *y*, and *z*) relative to the Castle Cove Fault plane. Permeability is plotted on a logarithmic scale. (c) Macrofracture densities binned into 5 m intervals from Debenham et al. (2018) and microfracture densities (per mm^2, this study) relative to distance from the fault. The grey shaded areas indicate areas where there is no outcrop and fractures could not be counted due to the presence of potential fault zones. Locations of synthetic faults and antithetic faults are also shown

consequently could not be used in this analysis. Mean permeabilities increase by two orders of magnitude from 0.04 mD at 225 m in the undeformed protolith to 1.26 mD at 0.5 m close to the fault plane. Within 0.5 m of the fault plane, permeabilities of up to 2.92 mD are recorded. Core plug permeabilities are plotted on a logarithmic scale relative to distance from the Castle Cove Fault plane (Figure 4b). Permeabilities are shown for three orientations (*x*, *y*, and *z*) relative to the Castle Cove Fault plane orientation. Permeabilities show a dispersed data spread for each core plug orientation at different distances to the fault plane, which may be attributed to micrometre-scale heterogeneities within the core plugs, such as microscopic sedimentary features that could not be avoided during sample collection. Permeabilities increase steadily from 225 to 64 m from the fault plane, and a peak is reached at 64 m. Similar to the porosity trend, permeabilities drop off to lower values at 37 m before increasing again toward the fault plane (Figure 4b) in the zone of maximum fracture density.

The relative proportions of oriented core plug permeabilities have been plotted on a ternary plot (Figure 5). At the greatest distance from the fault (225 m), there is minor permeability anisotropy with maximum permeability normal to the fault plane. The orientation of maximum permeability corresponds to sedimentary layers within the host rock.

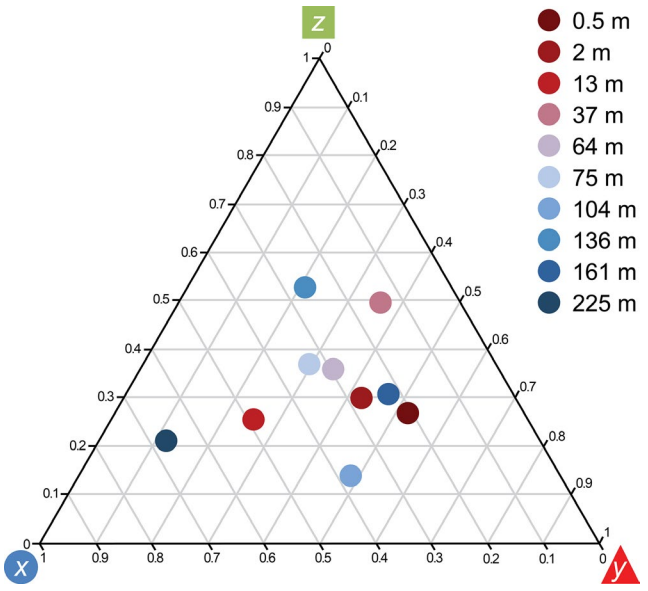

FIGURE 5 A triangle plot showing the ratios of mean core plug permeability. Core plugs in three orientations (*x*, *y*, and *z*) have been used for the identification of permeability anisotropy. Different colours indicate samples collected at different distances from the Castle Cove Fault

Permeabilities of the remaining samples are dispersed around the centre point of the ternary plot and do not show any clear relationship to orientation. This indicates that the core plugs

are relatively homogenous and do not have significant permeability anisotropy.

4.3 | Relationship between porosity and permeability

Core plug permeabilities are plotted on a logarithmic scale relative to core plug porosities (Figure 6). There is a strong positive correlation ($R^2 = 0.76$) between connected porosity and permeability (Figure 6). Porosity and permeability correlate with distance from the fault plane. For instance, core plugs taken from samples within the hanging wall anticline (<104 m from the fault plane) cluster in the higher porosity and permeability range than core plugs taken from samples beyond the hanging wall anticline (more than 104 m from the fault plane; Figure 6).

4.4 | Pore throat size and connectivity

Pore throat sizes are plotted on a logarithmic scale relative to pore volume (Figure 7a). Pore throat size distributions show a bimodal pattern with similar pore throat size peaks and pore volume frequencies in all samples; one peak includes pore throat sizes between 0.01–0.3 μm and a second peak between 0.3–1.5 μm (Figure 7a). At distance from the Castle Cove Fault plane (more than 104 m), there are greater volumes of smaller pore throat sizes (<0.3 μm). Closer to the fault plane, there is a shift to greater volumes of larger pore throat sizes (>1 μm; Figure 7a).

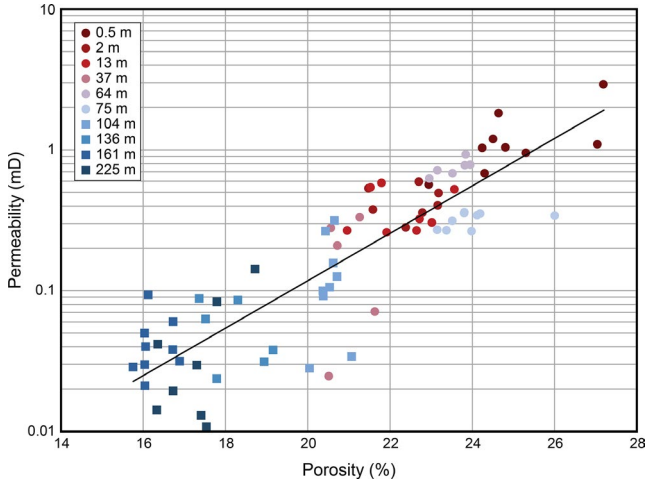

FIGURE 6 A cross plot of connected core plug porosity relative to core plug permeability. Permeability is plotted on a logarithmic scale. Different colours indicate samples collected at different distances from the Castle Cove Fault. Circles indicate samples collected within the Castle Cove Fault hanging wall anticline, whereas squares indicate samples collected beyond the hanging wall anticline. There is a strong positive correlation ($R^2 = 0.76$) between porosity and permeability

Mercury injection curves were used to determine the mercury threshold injection pressure in small offcuts of the core plugs. There is a strong negative correlation ($R^2 = 0.62$) between the threshold injection pressure of mercury and distance to the Castle Cove Fault plane; the threshold injection pressure decreases by one order of magnitude (from 216 to 56 psi) as the fault plane is approached (Figure 7b). Therefore, less pressure is required to form connected pathways between pores and saturate samples closer to the fault plane. Therefore, connectivity is better in more deformed rocks closer to the fault plane.

4.5 | Grain size

Grain size distributions were measured from 10 core plug sub-samples using laser diffraction (Figure 8a). The volumes of clay to coarse sand grains are plotted relative to distance to the Castle Cove Fault (Figure 8b). There is an overall increase in the volume of clay (moderate, $R^2 = 0.44$), silt (moderate, $R^2 = 0.53$), and very fine-sand (weak, $R^2 = 0.07$) grains (0.04–125 μm) in samples closer to the Castle Cove Fault, while there is an overall decrease in the volume of fine-sand (moderate, $R^2 = 0.44$), medium-sand (weak, $R^2 = 0.09$), and coarse-sand (weak, $R^2 = 0.09$) grains (125–2,000 μm) in samples away from the fault (Figure 8b). The volume of different grain sizes is mostly consistent until <37 m from the fault plane where there is a peak in fine sand and a decrease in clays to very fine sands (Figure 8b). While there is a weak to moderate linear relationship between the volumes of different grain size fractions relative to distance to the fault plane, these data indicate a progressive grain size reduction as the Castle Cove Fault plane is approached.

4.6 | Mineralogical observations

Within the hanging wall of the Castle Cove Fault, the Eumeralla Formation is a fine- to very fine-grained volcanogenic sandstone that is moderately sorted and compositionally immature. Mineral liberation analysis indicated that all samples have a similar mineralogical composition. The framework grains are predominantly lath-shaped to sub-rounded albite (up to 48 wt%) and angular to sub-rounded quartz (up to 27 wt%). Other minerals include potassium feldspar (present as orthoclase), kaolinite, illite, muscovite, biotite, accessory minerals (such as apatite and rutile), and coal fragments. Volcanic rock fragments typical of the Eumeralla Formation are mostly altered to diagenetic clays (Duddy, 2003; Tassone et al., 2014). Authigenic pore-lining chlorite (between 16 and 24 wt%) formed during early diagenesis is pervasive within all samples and the mean thickness of this lining is 10 μm. The pore-lining chlorite is characterised by two phases of crystallisation; a thick and poorly crystallised grain-coating chlorite that rims the

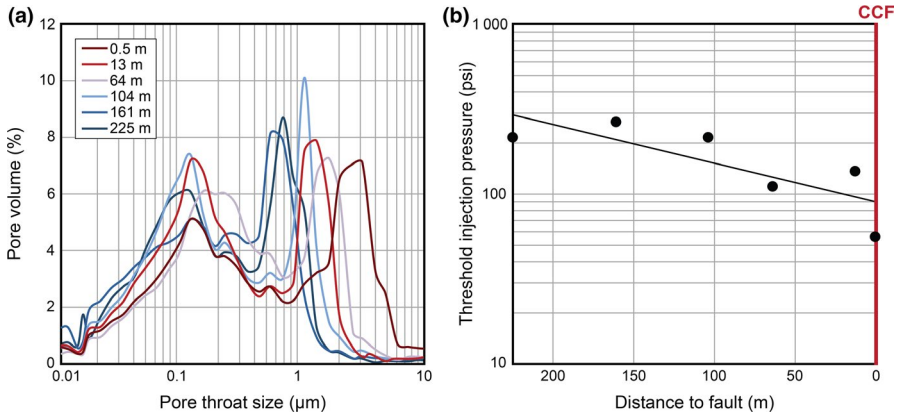

FIGURE 7 (a) Pore throat sizes plotted on a logarithmic scale relative to pore volume. Different colours indicate samples collected at different distances from the Castle Cove Fault. (b) The threshold injection pressure of mercury relative to distance to the Castle Cove Fault (CCF). Threshold injection pressure is plotted on a logarithmic scale. There is a strong negative correlation ($R^2 = 0.62$) between the threshold injection pressure of mercury and distance to the fault plane

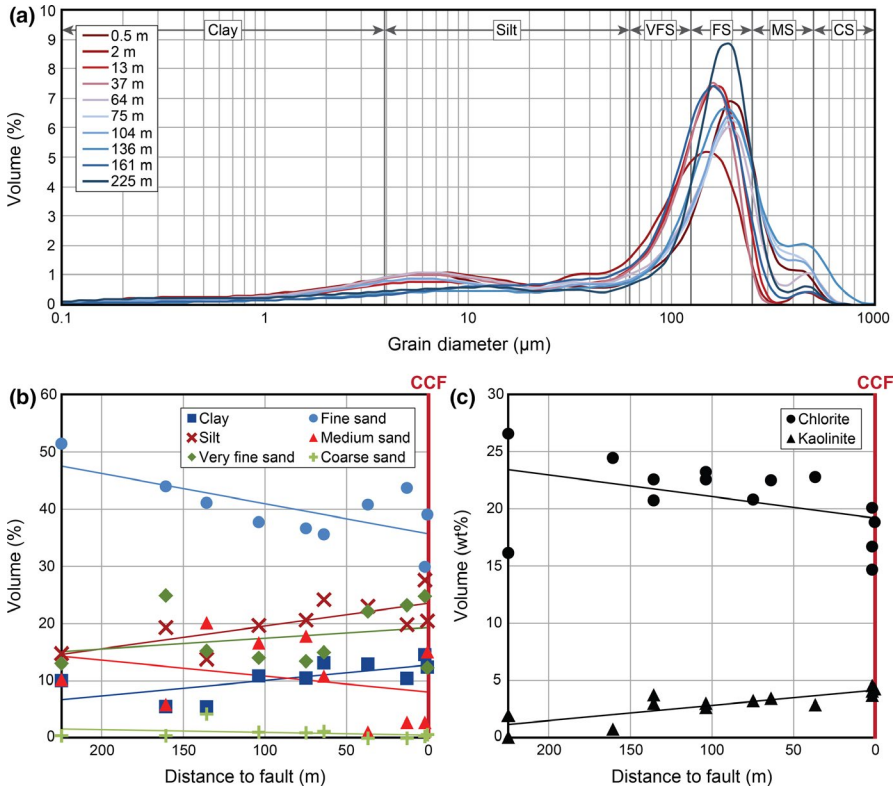

FIGURE 8 (a) Volume of grains relative to grain diameter identified in each sample. Different grain size (diameter) fractions are shown for clay, silt, very fine sand (VFS), fine sand (FS), medium sand (MS), and coarse sand (CS). (b) The volume of different grain sizes relative to distance to the Castle Cove Fault (CCF). Different symbols and colours indicate different grain sizes. (c) The volume of clays (chlorite and kaolinite) relative to distance to the Castle Cove Fault (CCF). Chlorite has a very weak negative correlation ($R^2 = 0.2$) with distance to the fault plane and kaolinite shows a strong positive correlation ($R^2 = 0.68$) with distance to the fault plane

grains, which transitions to a thin and well-crystallised euhedral pore-lining chlorite.

As the fault plane is approached, there is a change in the abundance of chlorite and kaolinite. For instance, chlorite decreases by ca. 4 wt% and kaolinite increases by ca. 2 wt% closer to the fault plane (Figure 8c). While chlorite has a very weak negative correlation ($R^2 = 0.2$) with distance to the fault plane, kaolinite shows a strong positive correlation ($R^2 = 0.68$) with distance (Figure 8c). Similarly, chlorite has a very weak negative correlation (porosity and permeability, $R^2 = 0.2$; Figure 9a, b), that is, porosity and permeability decrease with an increase in chlorite, while kaolinite shows a strong positive correlation (porosity, $R^2 = 0.57$; permeability $R^2 = 0.54$; Figure 9c, d), that is, porosity and permeability increase with an increase in kaolinite.

Diagenetic dissolution and replacement of detrital feldspars and volcanogenic clastics by albite and clays has changed the original framework composition of the Eumeralla Formation. Diagenetic albitization and kaolinization of orthoclase is extensive and some orthoclase grains are only partially albitized in a complex 'patchwork' pattern (Figure 10c, d). Within partially albitized orthoclase

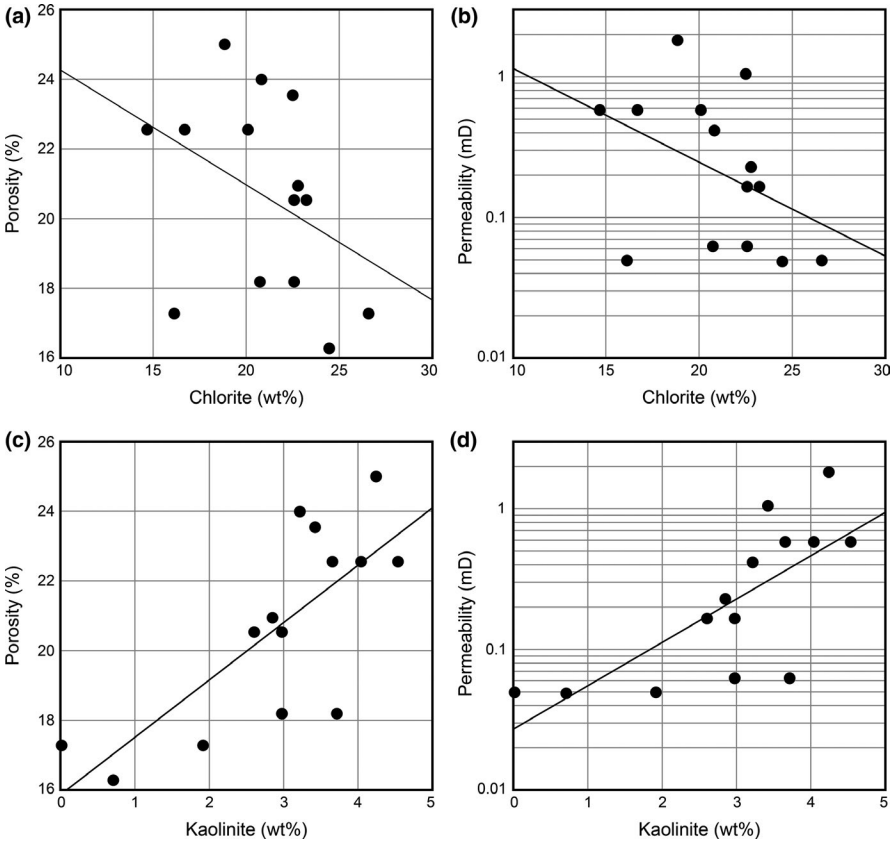

FIGURE 9 Relationship between volumes of clays relative to mean core plug porosity and permeability. Permeability is plotted on a logarithmic scale. (a) Chlorite relative to core plug porosity has a very weak negative correlation ($R^2 = 0.2$), and (b) chlorite relative to core plug permeability has a very weak negative correlation ($R^2 = 0.2$). (c) Kaolinite relative to core plug porosity has a strong positive correlation ($R^2 = 0.57$), and (d) kaolinite relative to core plug permeability has a strong positive correlation ($R^2 = 0.54$)

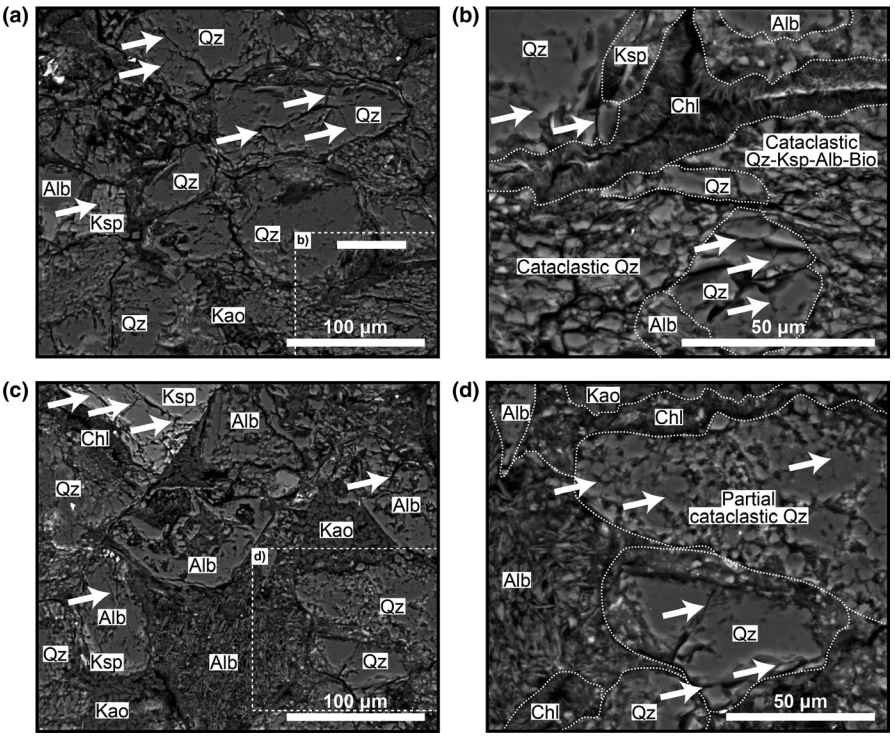

FIGURE 10 Backscattered *SEM* images of thin sections oriented in the *xz* plane at 2 m from the Castle Cove Fault plane. Larger grains of quartz and feldspar are deformed and fractured closer to the fault; examples of intragranular microfractures are indicated by the arrows. Evidence of cataclasis and subsequent grain size reduction, together with minor cataclasis of individual grains, is highlighted in (b) and (d). Diagenetic albitization and kaolinization of orthoclase is also evident in (b) and (d)

grains, small patches of quartz occur as a product of albitization (Baccar, Fritz, & Made, 1993). Some quartz grains are characterised by ragged textured characteristic of terminated quartz overgrowths (Figure 11c). There is also evidence for minor quartz dissolution by the presence of small (ca. 5 µm), irregular-shaped pits and voids that appear within detrital quartz grains. Within the quartz grains these occasionally coalesce to form larger voids and detached fragments of quartz.

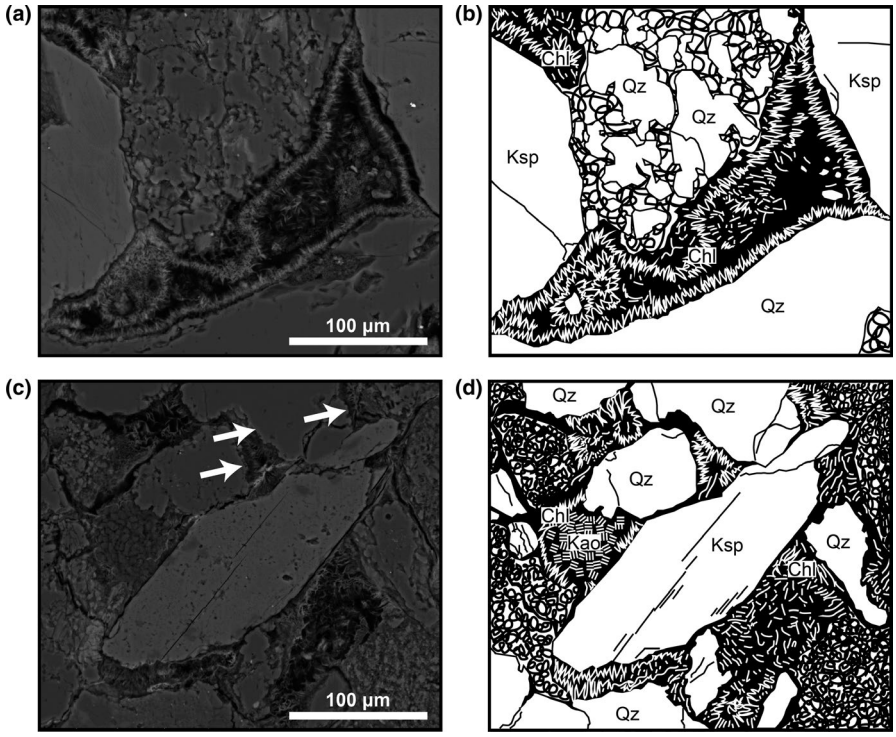

FIGURE 11 Backscattered *SEM* images of thin sections oriented in the *xz* plane, with schematic diagrams of the typical mineralogical and microstructural features identified within the Eumeralla Formation at Castle Cove. (a) Backscattered SEM images of 161 m from the Castle Cove Fault, and (b) schematic diagram of (a) showing well preserved intergranular porosity and filamentous pore-lining chlorite (Chl). Grains of quartz (Qz) and orthoclase (Ksp) have been identified. (c) Backscattered SEM images of 37 m from the Castle Cove Fault, and (d) schematic diagram of (c) showing a change in chlorite morphology (broken up and filling intergranular porosity) and increased microfractures within quartz and orthoclase grains. Terminated quartz overgrowth is present around some quartz grains. The diagenetic kaolinization of orthoclase in the form of kaolinite 'books' (Kao) is also shown

Orthoclase that has been kaolinized is evidenced by partial to full replacement of orthoclase grains by 'books' of kaolinite.

4.7 | Microstructural observations

Microstructural features were assessed at high resolutions using bSEM imaging. Microstructural image analysis on thin sections indicate that microfractures within the Castle Cove Fault damage zone are opening-mode (Mode I) fractures, as opposed to shear fractures (Mode II) identified at the outcrop scale (i.e. macrofractures) by Debenham et al. (2018). This indicates a scale-dependence on the types of fractures that form within the Castle Cove Fault damage zone. Microstructural analysis identified three structural processes that may have influenced the porosity and permeability structure of the sandstones within the Castle Cove Fault hanging wall. These processes include disaggregation of pore-lining chlorite, grain-scale cataclasis, and microfracturing (Figure 10). Away from the fault, intergranular porosity is strongly preserved by pore-lining chlorite (Figure 11a). However, closer to the fault the pore-lining chlorite is disaggregated and intergranular porosity is filled with chlorite plates (Figure 11c). Closer to the fault there is also increased deformation and minor cataclasis of individual grains (Figure 10). This may be controlling the progressive grain size reduction identified in laser diffraction particle size analysis.

Microstructural analysis showed a visual increase in microfracture densities closer to the Castle Cove Fault (Figure 11), from three microfractures per mm^2 at 225 m from the fault plane to 18 microfractures per mm^2 at 0.5 m from the fault plane (Figure 4c). In particular, larger grains of quartz and feldspar were deformed and fractured (Figures 10 and 11) closer to the fault. The number of microfractures within each counting area was consistent within each sample. Due to the diagenetic albitization and kaolinization of orthoclase, there will be an underestimation of microfracture density as diagenesis may have overprinted early-formed microfractures. This is mostly avoided by the microfracture counting method used in this study, which predominantly uses quartz grains to identify microfracture density changes. There is a strong positive correlation between the density of microfractures and porosity ($R^2 = 0.54$; Figure 12a) and the density of microfractures and permeability ($R^2 = 0.6$; Figure 12b). Microfractures are typically intragranular and transgranular, and in transmitted light microfractures appear to be open and do not contain cements. Goethite has precipitated within a small number of

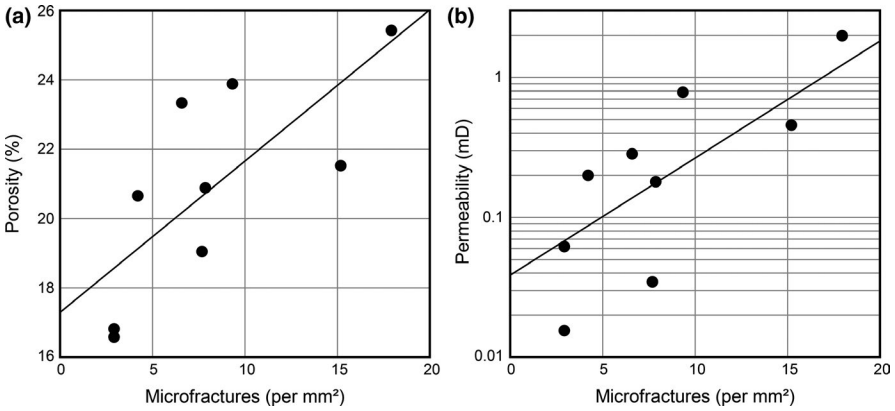

FIGURE 12 (a) The density of microfractures relative to mean core plug porosity has a strong positive correlation ($R^2 = 0.54$). (b) The density of microfractures relative to mean core plug permeability has a strong positive correlation ($R^2 = 0.6$). Permeability is plotted on a logarithmic scale

wider, grain-boundary microfractures (>10 μm). The orientations of the microfractures are typically variable within all samples (Figure 13). Grains with breccia-like microfractures were attributed to grain crushing as a result of compaction or artificial processes, such as sample preparation, and were avoided in this study.

5 | DISCUSSION

5.1 | Microfractures within the Castle Cove Fault damage zone

Microstructural analysis show that the density of microfractures increases toward the Castle Cove Fault plane (Figure 4c). These data show two main microfracture density peaks; the first peak is adjacent to a small fault zone (<20 m wide between 45 and 65 m from the Castle Cove Fault) and seems to be mainly influencing the sample at 64 m, and the second largest peak is adjacent to the Castle Cove Fault plane (Figure 4c). This positive relationship indicates that deformation, as a result of faulting, may be the main mechanism for microfracture formation. However, the microfractures do not exhibit preferential alignment to the Andersonian stresses associated with the Castle Cove Fault (Debenham et al., 2018). Microfractures are opening-mode (Mode I) fractures that are oriented parallel to the principal stress direction (Anders et al., 2014). Therefore, assuming that the microfractures formed during faulting, in the *xz* plane (Figure 3) the microfractures should appear: (a) vertical, with an Andersonian vertical maximum principal stress axis (i.e. gravity) during normal faulting, and (b) horizontal and perpendicular to the horizontal maximum principal stress, with an Andersonian horizontal maximum principal stress axis during reverse faulting (Anderson, 1951; Debenham et al., 2018). Given the variable microfracture orientations (Figure 13), other processes may have also contributed to the formation of microfractures.

Structural processes such as stress heterogeneity, rotation, and changes in concentration around a fault can influence the microfracture fabric of the damage zone (Bell, 1996; Wilson, Chester, & Chester, 2003), and these could explain the variable

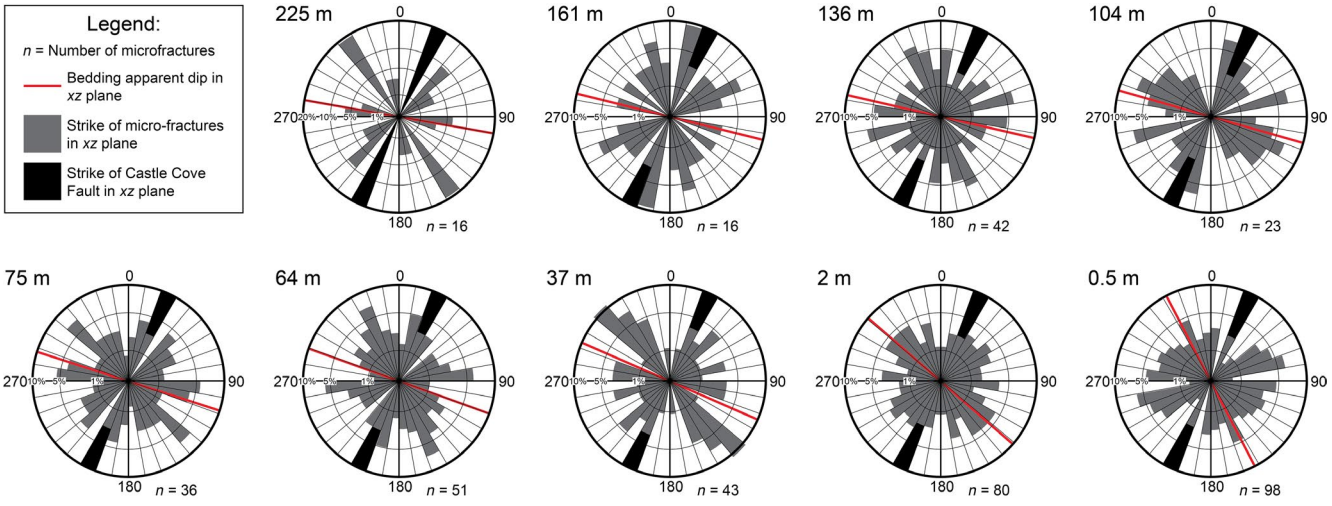

FIGURE 13 Equal area-scaled rose diagrams showing microfracture orientations at different distances from the Castle Cove Fault. The area of each sector of the rose diagram is proportional to the frequency of microfracture orientations (Nemec, 1988) and each petal represents 10° angle increments. Microfractures were identified in thin sections oriented in the *xz* plane. The orientation, that is, apparent dip, of the bedding relative to the *xz* plane cross-section is illustrated by the thick red line

microfracture orientations observed in this study. Anticlinal folding in the hanging wall may have contributed to the formation of microfractures (Zeng, 2010). Microfractures formed during normal movement of the Castle Cove Fault and associated rollover folding in the hanging wall would have subsequently been tilted and re-oriented during amplification of the fold during reverse-reactivation. Therefore, the present day orientations of microfractures associated with the normal movement of the fault will not appear Andersonian. Other processes that can be attributed to the formation of variably oriented microfractures include; (a) pre-depositional processes, that is, the microfractures may be inherited from the original source rock of the sediments (Laubach, 1997); (b) syn-diagenetic processes, that is, microfractures formed during diagenesis due to compaction and subsequent cement precipitation (Boggs & Krinsley, 2006); (c) near-surface processes, that is, weathering; or (d) artificial processes, that is, damage during thin section cutting and polishing, which was avoided as much as possible.

There are a number of processes that can lead to the formation of microfractures, and the application of analytical methods, such as three-dimensional microfracture imaging or *SEM*-based cathodoluminescence imaging, could further resolve these processes (Laubach, 1997; Milliken & Laubach, 2000). While a number of processes are contributing to microfracture formation, a comprehensive analysis of these is beyond the scope of this study; rather, this study assesses changes in microfracture density and dip orientation relative to distance to the fault plane.

5.2 | The relationship between clays and the permeability structure of the Eumeralla Formation

At Castle Cove, the abundance of chlorite is mostly consistent throughout the sampled areas. Chlorite decreases by ca. 4 wt% as the Castle Cove Fault plane is approached, but only shows a weak correlation with distance (Figure 8c). Within the Eumeralla Formation, porosity is strongly preserved by authigenic pore-lining chlorite formed during early diagenesis. The early precipitation of pore-lining chlorite has also prevented extensive quartz overgrowth and quartz grains that are rimmed by secondary quartz overgrowths are typically terminated by the growth of chlorite (Figure 11). While the pore-lining chlorite presents potentially negative ramifications for reservoir quality, such as the closure of pore throats and subsequent reduction in permeability, deformation associated with faulting has broken up and disaggregated the authigenic chlorite closer to the Castle Cove Fault to improve the micrometre-scale permeability structure. More specifically, when the pore-lining chlorite is disaggregated during deformation, the chlorite will: (a) fill the pore space and reduce porosity slightly and (b) open up pore-throats and increase micrometre-scale permeability and connectivity.

The abundance of kaolinite is also mostly consistent across the study area. Kaolinite increases by ca. 2 wt% and has a strong positive correlation as the fault plane is approached (Figure 8c). Similarly, kaolinite shows a strong positive correlation with porosity and permeability (Figure 9c, d). As kaolinite only increases by a small volume as the fault plane is approached and there is evidence for the kaolinization of orthoclase, it is likely that an increase in permeability due to microfracturing is driving the precipitation of kaolinite. The precipitation of authigenic kaolinite is generally related to the presence of meteoric waters (Lanson et al., 2002). An enhanced micrometre-scale permeability structure closer to the Castle Cove Fault would provide the necessary fluid flow conduits for this reaction to occur. This suggests that an enhanced permeability structure due to faulting is leading to increased diagenesis and alteration of the protolith adjacent to the fault plane. Mineralogical changes due to diagenesis will consequently alter the mechanical properties of the protolith (Laubach, Olson, & Gross, 2009). Diagenesis may also alter the petrophysical properties of the protolith through the precipitation of minerals and occlusion of pore space (e.g. heal microfractures) or the dissolution of minerals and creation of pore space (e.g. intragranular porosity; Pittman, 1979).

5.3 | Enhancement of micrometre-scale permeability structure closer to the fault plane

A positive relationship between the petrophysical properties of the host rock and distance toward the Castle Cove Fault plane has been observed (Figure 14). The porosity, permeability, and microstructural data show two main peaks (Figure 4). The first peak is adjacent to a small fault zone (between 45 and 65 m) and shows enhanced petrophysical properties for samples at 64 and 75 m from the Castle Cove fault. The second and largest peak is adjacent to the Castle Cove Fault plane, within the zone of maximum fracture density, and the petrophysical properties of all samples in the damage zone are influenced by this fault. The zone of maximum fracture density is a zone of increased deformation within the damage zone adjacent to the Castle Cove Fault. Increased deformation within this zone would have a greater influence on the enhancement on not only the macroscale permeability structure of the damage zone (Debenham et al., 2018), but also the micrometre-scale permeability structure of the damage zone. Consistently high connected porosities (Figure 4a) and permeabilities (Figure 4b) due to elevated microfracture densities (Figure 4c) and grain-scale cataclasis (Figure 10) within this zone demonstrate this.

Overall, porosity and permeability at ambient pressures increase as the Castle Cove Fault plane is approached (Figures 4 and 14). Pore throat sizes also increase closer to the fault plane and connectivity is improved as a result (Figure 7). However, there is a reduction in grain size as the fault plane

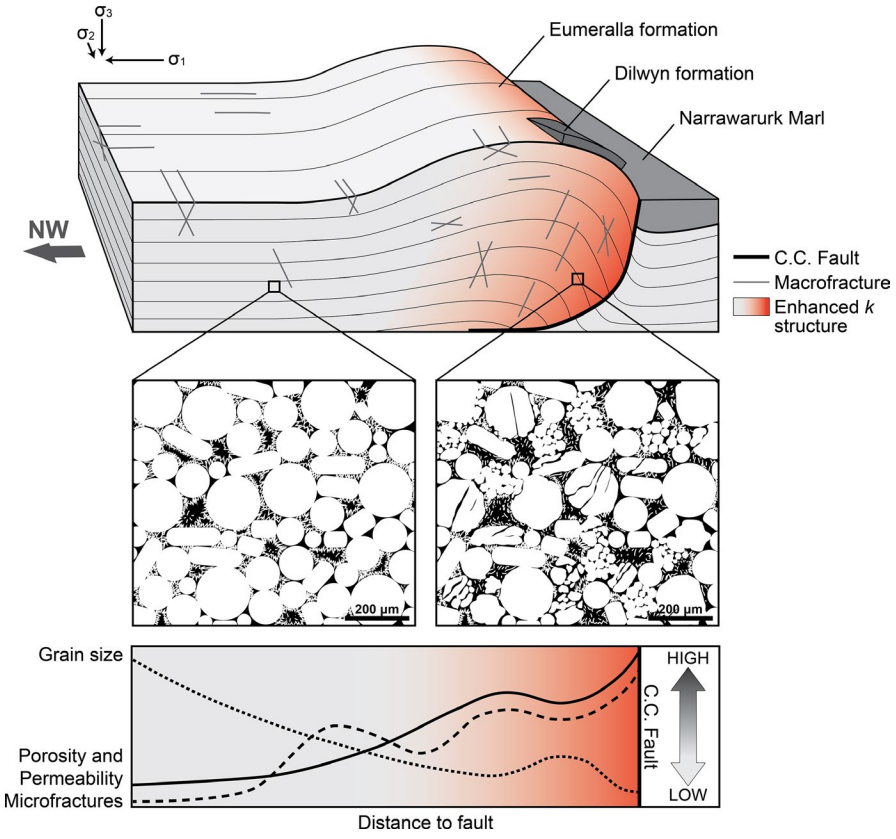

FIGURE 14 A summary model of the petrophysical properties of the Castle Cove Fault damage zone within the hanging wall. The block diagram illustrates the present day configuration of the Castle Cove outcrop, with macrofracture orientations from Debenham et al. (2018). This model shows an enhanced permeability structure associated with complex deformation from the Castle Cove Fault. The bottom graph summarises the porosity, permeability, macrofracture count, and grain size data from this study, where porosity, permeability, and number of macrofractures increase toward the fault and grain size decreases toward the fault

is approached and the volume of clays to very fine-grained sands increases toward the fault (Figures 8 and 14). It would be expected that this would have a detrimental effect on the petrophysical properties of the host rock. However, there is a positive relationship between the petrophysical properties and distance to the fault plane. Therefore, other factors must be influencing the enhancement of the petrophysical properties of the host rock.

Thin section analyses indicate that the larger pore throat sizes measured in mercury-intrusion porosimetry can be attributed to the presence of microfractures and intergranular porosity preserved by pore-lining chlorite. Smaller pore throat sizes likely represent microporosity between clays, particularly within the filamentous and porous pore-lining chlorite. Microstructural analysis at the grain-scale has demonstrated that the density of microfractures correlates strongly with changes in porosity and permeability (Figures 12 and 14). This indicates that an increase in connectivity adjacent to the Castle Cove Fault is related to an increase in microfractures. A change in the morphology of pore-lining chlorite, that is, well-structured away from the fault to broken up and disaggregated adjacent to the fault, may also contribute to enhanced connectivity (Figures 11 and 14). The increase in connected porosity toward the fault plane is attributed to the increase in microfracturing (Figure 12a) and disaggregation of pore-lining chlorite, and this explains the strong correlation between connected porosity and permeability (Figure 6). Despite an enhancement of the micrometre-scale permeability structure within the Castle Cove Fault damage zone, the petrophysical properties of this interval of the Eumeralla Formation indicate that the formation has the properties of a tight reservoir (i.e. permeabilities typically <1 mD).

5.4 | Comparison of the permeability structure described in this study to other studies

Many investigations into the permeability structure of fault zones with simple tectonic histories have been undertaken on low porosity host rocks such as granites, mylonites, schists, and low porosity sandstones (Balsamo, Storti, Salvini, Silva, & Lima, 2010; Cavailhes et al., 2013; Evans, Forster, & Goddard, 1997; Mitchell & Faulkner, 2012; Wibberley & Shimamoto, 2003) and porous sandstones (Antonellini & Aydin, 1994; Farrell et al., 2014; Shipton et al., 2002). However, studies on the influence of complex faults with multi-slip histories on the permeability structure of porous rocks are limited. It is widely recognised that the primary intrinsic control on permeability structure is the lithology of the protolith. The lithology will influence the types of fault-related deformation processes that can occur within a host rock, therefore influencing permeability structure.

Studies of fault-bearing porous sandstones have identified a number of fault-related deformation processes influencing

permeability structure. Shipton et al. (2002) analysed the permeability structure of Jurassic-aged porous sandstones (Navajo Sandstone) that are intersected by a normal fault (Big Hole Fault) in Utah, western United States. The Big Hole Fault has a strike length of 4.1 km and fault throw is between 3 to 29 m (Shipton & Cowie, 2001). Shipton et al. (2002) demonstrated that centimetre- to metre-scale deformation (e.g. the formation of deformation bands), associated with faulting resulted in a decline in porosity (20% to <10%) and permeability (more than 2,000 mD to <0.1 mD) as the fault is approached. A detailed study was also undertaken by Farrell et al. (2014) on Permo-Triassic porous sandstones (Hopeman Sandstone Formation) within the damage zone of a normal fault (Clashach Fault). The Clashach Fault has a strike length over 1 km and fault throw is up to 50 m (Farrell et al., 2014). While the bulk permeability of the host rock decreases as the fault plane is approached, they explained that permeability anisotropy, that is, preferentially oriented pore connectivity, is created as a result of faulting. Within these sandstones, permeability anisotropy is controlled by the formation of elongated pores and microfractures related to faulting, with maximum permeability oriented parallel to fault plane dip.

Unlike the faulting-related permeability structures described by Shipton et al. (2002) and Farrell et al. (2014), the results from this study show an increase in the bulk petrophysical properties of the host rock as the Castle Cove Fault plane is approached. This highlights the significant variability that faults can have on the permeability structure of fault zones in porous sandstones. The development of permeability anisotropy as a result of faulting is also not observed at Castle Cove. Minor permeability anisotropy is observed away from the fault (225 m; Figure 5) and this is attributed to the orientation of the bedding relative to the core plugs, that is, core plugs with permeability anisotropy are approximately parallel to bedding (Figure 2c, d). Therefore, fine laminations and millimetre-scale coal seams within this interval of the Eumeralla Formation are controlling permeability anisotropy. The remaining samples do not show permeability anisotropy and there are a few reasons for this. For instance, the absence of preferentially oriented microfractures and pore fabrics from deformation would result in variable permeabilities. This is considered to be the main control on the isotropy of permeability. Second, a broad anticline (ca. 80 m in half-wavelength) in the hanging wall has tilted the beds adjacent to the Castle Cove Fault (Figure 2). The geometry of the beds and fine laminations will influence the direction of permeability anisotropy, and as the core plugs have been drilled at an angle that is not parallel to bedding within the anticline, permeability anisotropy caused by bedding may not be identified during core plug permeability and porosity analysis. Anticlinal folding within the hanging wall of the Castle Cove Fault is an expression of a complex structural regime. Therefore, both the protolith and the structural history of the fault have influenced the permeability structure at Castle Cove.

This study describes the influence of a reverse-reactivated fault on the damage zone permeability structure of the Eumeralla Formation. Normal faulting of the Castle Cove Fault and subsequent reactivation as a reverse fault has resulted in complex deformation within the hanging wall at a range of scales, which in turn has influenced the development of the permeability structure. For instance, at the outcrop-scale, anticlinal folding in the hanging wall associated with the reversal of the Castle Cove Fault has tilted the beds and fine laminations. This would influence the direction of permeability anisotropy, as described above. Also at the outcrop-scale, the formation of macrofractures related to the multiple-slip history of the Castle Cove Fault (Debenham et al., 2018) has provided an extensive permeability network. At the micrometre-scale, the formation of variably oriented microfractures is attributed to the multiple-slip history of the fault, along with other processes as discussed previously. Complex deformation associated with normal faulting followed by reverse faulting has influenced the off-fault fluid flow properties of the host rock.

5.5 | Implications for fluid flow and fluid exploration in sedimentary basins

Using insights from the Castle Cove Fault, this study aims to understand the influence of inverted faults on the micrometre-scale permeability structure, and therefore fluid flow, within tight sandstones, which are growing targets for fluid extraction and storage in sedimentary basins. The main implications for fluid flow and fluid exploration adjacent to reverse-reactivated faults are summarised here; (a) Enhanced deformation adjacent to the fault plane results in the formation of variably oriented microfractures that leads to isotropic permeability. While fluid flow is increased adjacent to the fault plane, fluid flow may occur in any direction. (b) Where pore-lining clays are present (e.g. chlorite, illite, and montmorillonite; Neasham, 1977), disaggregation of the clays due to deformation can enhance the micrometre-scale permeability structure of the protolith by opening pore-throats. However, porosity can be reduced as the disaggregated clays fill pore space during deformation and this may impede fluid flow. (c) Enhanced deformation adjacent to the fault plane results in the cataclasis of individual grains (i.e. grain size reduction) which can reduce the connected pore space, therefore impeding fluid flow (Antonellini & Aydin, 1994). (d) At the outcrop scale, the reverse-reactivation of normal faults often results in anticlinal folding and uplift in the hanging wall, which would form structural highs acting as traps for fluids (c.f. Debenham et al., 2018). Alternatively, folding and uplift during inversion may result in changes in

pre-existing trap configurations, thereby increasing the risk of fluid leakage (Cooper & Warren, 2010). Characterisation of the micrometre-scale permeability structure adjacent to reverse-reactivated faults will aid with predicting fluid flow associated with such inversion structures.

5.6 | Application of results, upscaling issues, and further work

Farrell et al. (2014) described the parameters considered to be suitable for measuring the petrophysical properties of core plugs. The use of multiple core plugs with an average core plug volume of 32.7 cm^3 is deemed to be valid for repeatable and representative results and for assessing micrometre-scale features in this study. While core plugs can be used to assess the micrometre-scale petrophysical properties of the host rock, they exclude the petrophysical properties associated with large-scale features such as macrofractures and deformation bands. On the contrary, conventional reservoir modelling workflows typically exclude the effects of micrometre-scale heterogeneity. Therefore, multiple datasets need to be considered when describing the field-scale permeability structure of a fault damage zone.

While the petrophysical properties (e.g. porosity, permeability, and pore connectivity) of the Eumeralla Formation at Castle Cove were enhanced as a result of fault-related deformation, the host rock is still considered to be a tight sandstone (i.e. a reservoir rock with permeabilities of <1 mD and as low as 0.001 mD; Kazemi, 1982). Consequently, in order for the Castle Cove Fault damage zone to be an effective conduit for significant fluid flow, the presence of large-scale features such as macrofractures and small-scale faults are required. A complex macrofracture network exists at Castle Cove, with three fracture sets identified to be geometrically related to the Castle Cove Fault (Debenham et al., 2018). Depending on the timing of macrofracture formation and reactivation relative to fluid flow, it is expected that these would act as more effective conduits for fluid flow than the bulk permeability of the host rock. Integrating macrofracture densities associated with the Castle Cove Fault into reservoir modelling workflows would account for bulk permeability.

To further improve the applicability of the results from this study to reservoir models, it would be beneficial to carry out additional laboratory experiments under conditions that are representative of in situ temperature and confining pressure conditions. Moreover, although the Castle Cove Fault is not exposed at the surface, an investigation into the internal structure of the fault, for example, fault core and peripheral damage zone, would result in a better understanding of the permeability structure of the Castle Cove Fault. It is also important to note that the Eumeralla Formation is lithologically variable and is characterised by different zones of diagenetic alteration (Duddy, 2002) and porosity reduction as a result of over-compaction during burial (Tassone et al., 2014), and therefore the permeability structure may vary considerably depending on position in stratigraphy. While this study only focusses on the upper interval of the Eumeralla Formation, our results can be used as an analogue for sandstones that are characterised by high porosities, low permeabilities, and abundant clays.

This study highlights the importance of undertaking detailed petrophysical, structural, and mineralogical analyses of reservoir rocks that have experienced complex deformation associated with faulting. Within the hanging wall of an inverted fault, microstructural changes as a result of faulting-induced deformation have enhanced the micrometre-scale permeability structure. This study has significant implications for the future development of robust exploration and fluid monitoring strategies of similar faults in the eastern Otway Basin which have experienced similar deformation histories and other analogous faults globally.

6 | CONCLUSIONS

High resolution petrophysical, microstructural, and mineralogical analyses have been undertaken on porous sandstones that have experienced complex faulting. The results from this study show that microstructural changes as a result of faulting have improved the permeability structure of the Eumeralla Formation within the hanging wall of the Castle Cove Fault:

- As the fault plane is approached, connected porosity increases by 10% and permeability at ambient pressures increases by two orders of magnitude. Pore throat sizes also increase closer to the fault plane and connectivity is improved as a result. However, there is a reduction in grain size toward the fault. An improvement of the permeability structure toward the fault plane reflects an opposite trend to other fault zones (e.g. Big Hole Fault and Clashach Fault) compared in this study. This highlights the significant variability that faults can have on the permeability structure of fault zones in porous sandstones.
- Detailed thin section analyses indicate that the larger pore throat sizes measured in mercury-intrusion porosimetry can be attributed to the presence of microfractures and intergranular porosity preserved by pore-lining chlorite.
- Microstructural analysis at the grain-scale has demonstrated that the density of microfractures correlates strongly with changes in connected porosity and permeability. This indicates that an increase in connectivity adjacent to the Castle Cove Fault is related to an increase in microfractures.
- Destruction of original authigenic pore-lining chlorite morphology may also contribute to enhanced connectivity.

Despite improvement of the permeability structure, the upper Eumeralla Formation at Castle Cove is still considered a tight sandstone. However, the extensive macrofracture network described in Debenham et al. (2018) could act as a conduit for significant fluid flow in this system. This study shows that high-resolution analyses of the protolith are fundamental for describing the permeability structure of reservoir rocks with high porosities, low permeabilities, and abundant clays. This study also has significant implications for future exploration and fluid monitoring strategies within reservoir rocks that have experienced complex structural histories.

ACKNOWLEDGEMENTS

This research forms part of a PhD project supported by the Australian Research Council [Discovery Project DP160101158] and through an Australian Government Research Training Program Scholarship. Dave Healy acknowledges the support of the Natural Environment Research Council (NERC, UK) through the award NE/N003063/1 'Quantifying the Anisotropy of Permeability in Stressed Rock'. This study was also funded by scholarships from the Petroleum Exploration Society of Australia and the Australian Petroleum Production and Exploration Association. We thank Gordon Holm for preparing thin sections and Colin Taylor for carrying out particle size measurements and mercury injection capillary pressure analyses. Aoife McFadden and David Kelsey from Adelaide Microscopy, Braden Morgan, and Sophie Harland are acknowledged for their assistance with laboratory work. Field assistants James Hall, Rowan Hansberry, and Lachlan Furness are also gratefully acknowledged for their assistance with sample collection. Discussions with Ian Duddy on the mineralogy of the Eumeralla Formation are also greatly appreciated. This forms TRaX record 416.

ORCID

Natalie Debenham https://orcid.org/0000-0001-8896-8582

Natalie J. C. Farrell https://orcid.org/0000-0002-8491-9094

Simon P. Holford https://orcid.org/0000-0002-4524-8822

Rosalind C. King https://orcid.org/0000-0001-9160-996X

David Healy https://orcid.org/0000-0003-2685-1498

REFERENCES

Anders, M. H., Laubach, S. E., & Scholz, C. H. (2014). *Microfractures: A Review. Journal of Structural Geology 69(Part, B)*, 377–394. https://doi.org/10.1016/j.jsg.2014.05.011

Anderson, E. M. (1951). *The dynamics of faulting and dyke formation with applications to Britain*, 2nd ed. Edinburgh, UK: Oliver and Boyd.

Antonellini, M., & Aydin, A. (1994). Effect of faulting on fluid flow in porous sandstones: Petrophysical properties. *AAPG Bulletin*, *78*, 355–377.

Aydin, A. (2000). Fractures, faults, and hydrocarbon entrapment, migration and flow. *Marine and Petroleum Geology*, *17*, 797–814. https://doi.org/10.1016/S0264-8172(00)00020-9

Baccar, M. B., Fritz, B., & Made, B. (1993). Diagenetic albitization of K-feldspar and plagioclase in sandstone reservoirs; thermodynamic and kinetic modeling. *Journal of Sedimentary Research*, *63*, 1100–1109. https://doi.org/10.1306/D4267CB2-2B26-11D7-8648000102C1865D

Balsamo, F., Storti, F., Salvini, F., Silva, A. T., & Lima, C. C. (2010). Structural and petrophysical evolution of extensional fault zones in low-porosity, poorly lithified sandstones of the Barreiras Formation, NE Brazil. *Journal of Structural Geology*, *32*, 1806–1826. https://doi.org/10.1016/j.jsg.2009.10.010

Bauer, J. F., Meier, S., & Philipp, S. L. (2015). Architecture, fracture system, mechanical properties and permeability structure of a fault zone in Lower Triassic sandstone, Upper Rhine Graben. *Tectonophysics*, *647–648*, 132–145. https://doi.org/10.1016/j.tecto.2015.02.014

Bell, J. S. (1996). In situ stresses in sedimentary rocks (part 2): Applications of stress measurements. *Geoscience Canada*, *23*, 135–153.

Bense, V. F., Gleeson, T., Loveless, S. E., Bour, O., & Scibek, J. (2013). Fault zone hydrogeology. *Earth-Science Reviews*, *127*, 171–192. https://doi.org/10.1016/j.earscirev.2013.09.008

Bense, V. F., & Person, M. A. (2006). Faults as conduit-barrier systems to fluid flow in siliciclastic sedimentary aquifers. *Water Resources Research*, *42*(5), 1–18. https://doi.org/10.1029/2005WR004480

Blott, S. J., Croft, D. J., Pye, K., Saye, S. E., & Wilson, H. E. (2004). Particle size analysis by laser diffraction. *Geological Society, London, Special Publications*, *232*, 63–73. https://doi.org/10.1144/gsl.sp.2004.232.01.08

Boggs, S., & Krinsley, D. (2006). Cathodoluminescence and its causes. In D. Krinsley, & S. Boggs (Eds.), *Application of cathodoluminescence imaging to the study of sedimentary rocks* (pp. 7–18). Cambridge, UK: Cambridge University Press.

Boreham, C. J., Hope, J. M., Jackson, P., Davenport, R., Earl, K. L., Edwards, D. S., … Krassay, A. A. (2004). Gas-oil-source correlations in the Otway Basin. In P. J. Boult, D. R. Johns, & S. C. Lang (Eds.), *Eastern Australian Basins Symposium II. Petroleum Exploration Society of Australia Special Publication* (pp. 97–106).

Bredehoeft, J. D. (1997). Fault permeability near Yucca Mountain. *Water Resources Research*, *33*, 2459–2463. https://doi.org/10.1029/97WR01710

Caine, J. S., Evans, J. P., & Forster, C. B. (1996). Fault zone architecture and permeability structure. *Geology*, *24*, 1025–1028. https://doi.org/10.1130/0091-7613(1996) 024<1025:fzaaps>2.3.co;2

Cavailhes, T., Sizun, J.-P., Labaume, P., Chauvet, A., Buatier, M., Soliva, R., … Gout, C. (2013). Influence of fault rock foliation on fault zone permeability: The case of deeply buried arkosic sandstones (Gres d'Annot, southeastern France). *AAPG Bulletin*, *97*, 1521–1543. https://doi.org/10.1306/03071312127

Cooper, M. A., & Warren, M. J. (2010). The geometric characteristics, genesis and petroleum significance of inversion structures.

Geological Society, London, Special Publications, *335*, 827–846. https://doi.org/10.1144/sp335.33

Debenham, N., King, R. C., & Holford, S. P. (2018). The influence of a reverse-reactivated normal fault on natural fracture geometries and relative chronologies at Castle Cove, Otway Basin. *Journal of Structural Geology*, *112*, 112–130. https://doi.org/10.1016/j.jsg.2018.05.004

Duddy, I. R. (1994). *The Otway Basin: Thermal, structural, tectonic and hydrocarbon generation histories*. NGMA/PESA Otway Basin Symposium, Melbourne (pp. 35–42).

Duddy, I. R. (2002). *The Otway Basin: Geology, sedimentology, diagenesis, AFTA thermal history reconstruction and hydrocarbon prospectivity. Field Trip Guide prepared for the National Centre for Petroleum Geology and Geophysics, Adelaide*. Geotrack International Pty. Ltd.

Duddy, I. R. (2003). Mesozoic: A time of change in teconic regime. In W. D. Birch (Ed.), *Geology of Victoria*. GSA Special Publication 23 (pp. 239–286).

Edwards, D. S., Struckmeyer, H. I. M., Bradshaw, M. T., & Skinner, J. E. (1999). Geochemical characteristics of Australia's southern margin petroleum systems. *The APPEA Journal*, *39*, 297–321. https://doi.org/10.1071/AJ98017

Edwards, J., Leonard, J. G., Pettifer, G. R., & Mcdonald, P. A. (1996). Colac 1: 250000 Map Geological Report. Report 98. Geological Survey.

Evans, J. P., Forster, C. B., & Goddard, J. V. (1997). Permeability of fault-related rocks, and implications for hydraulic structure of fault zones. *Journal of Structural Geology*, *19*, 1393–1404. https://doi.org/10.1016/S0191-8141(97)00057-6

Fairley, J. P. (2009). Modeling fluid flow in a heterogeneous, fault-controlled hydrothermal system. *Geofluids*, *9*, 153–166. https://doi.org/10.1111/j.1468-8123.2008.00236.x

Farrell, N. J. C., & Healy, D. (2017). Anisotropic pore fabrics in faulted porous sandstones. *Journal of Structural Geology*, *104*, 125–141. https://doi.org/10.1016/j.jsg.2017.09.010

Farrell, N. J. C., Healy, D., & Taylor, C. W. (2014). Anisotropy of permeability in faulted porous sandstones. *Journal of Structural Geology*, *63*, 50–67. https://doi.org/10.1016/j.jsg.2014.02.008

Faulkner, D. R., Jackson, C., Lunn, R. J., Schlische, R. W., Shipton, Z. K., Wibberley, C., & Withjack, M. O. (2010). A review of recent developments concerning the structure, mechanics and fluid flow properties of fault zones. *Journal of Structural Geology*, *32*, 1557–1575. https://doi.org/10.1016/j.jsg.2010.06.009

Fisher, Q. J., & Knipe, R. J. (1998). Fault sealing processes in siliciclastic sediments. *Geological Society, London, Special Publications*, *147*, 117–134. https://doi.org/10.1144/gsl.sp.1998.147.01.08

Folch, A., & Mas-Pla, J. (2008). Hydrogeological interactions between fault zones and alluvial aquifers in regional flow systems. *Hydrological Processes*, *22*, 3476–3487. https://doi.org/10.1002/hyp.6956

Fossen, H., Schultz, R. A., Shipton, Z. K., & Mair, K. (2007). Deformation bands in sandstone: A review. *Journal of the Geological Society*, *164*, 755–769. https://doi.org/10.1144/0016-76492006-036

Holford, P., Tuitt, A. K., Hillis, R. R., Green, P. F., Stoker, M. S., Duddy, I. R., … Tassone, D. R. (2014). Cenozoic deformation in the Otway Basin, southern Australian margin: Implications for the origin and nature of post-breakup compression at rifted margins. *Basin Research*, *26*, 10–37. https://doi.org/10.1111/bre.12035

Katz, A. J., & Thompson, A. H. (1987). Prediction of rock electrical conductivity from mercury injection measurements. *Journal of Geophysical Research: Solid Earth*, *92*, 599–607. https://doi.org/10.1029/JB092iB01p00599

Kazemi, H. (1982). Low-permeability gas sands. *Journal of Petroleum Technology*, *34*, 2229–2232. https://doi.org/10.2118/11330-PA

Klinkenberg, L. J. (1941). *The permeability of porous media to liquids and gases* (pp. 200–213). American Petroleum Institute, Drilling and Production Practice.

Knipe, R. J., Jones, G., & Fisher, Q. J. (1998). Faulting, fault sealing and fluid flow in hydrocarbon reservoirs: An introduction. *Geological Society, London, Special Publications*, *147*, vii–xxi. https://doi.org/10.1144/gsl.sp.1998.147.01.01

Krassay, A. A., Cathro, D. L., & Ryan, D. J. (2004). A regional tectonostratigraphic framework for the Otway Basin. In P. J. Boult, D. R. Johns, & S. C. Lang (Eds.), *Eastern Australian Basins Symposium II* (pp. 97–106). Petroleum Exploration Society of Australia Special Publication.

Lanson, B., Beaufort, D., Berger, G., Bauer, A., CassagnabèRe, A., & Meunier, A. (2002). Authigenic kaolin and illitic minerals during burial diagenesis of sandstones: A review. *Clay Minerals*, *37*, 1–22. https://doi.org/10.1180/0009855023710014

Laubach, S. E. (1997). A method to detect natural fracture strike in sandstones. *AAPG Bulletin*, *81*, 604–623.

Laubach, S. E., Olson, J. E., & Gross, M. R. (2009). Mechanical and fracture stratigraphy. *AAPG Bulletin*, *93*, 1413–1426. https://doi.org/10.1306/07270909094

Milliken, K. L., & Laubach, S. E. (2000). Brittle deformation in sandstone diagenesis as revealed by scanned cathodoluminescence imaging with application to characterization of fractured reservoirs. In M. Pagel, V. Barbin, P. Blanc, & D. Ohnenstetter (Eds.), *Cathodoluminescence in geosciences* (pp. 225–243). Berlin Heidelberg: Springer Berlin Heidelberg.

Mitchell, T. M., & Faulkner, D. R. (2009). The nature and origin of off-fault damage surrounding strike-slip fault zones with a wide range of displacements: A field study from the Atacama fault system, northern Chile. *Journal of Structural Geology*, *31*, 802–816. https://doi.org/10.1016/j.jsg.2009.05.002

Mitchell, T. M., & Faulkner, D. R. (2012). Towards quantifying the matrix permeability of fault damage zones in low porosity rocks. *Earth and Planetary Science Letters*, *339–340*, 24–31. https://doi.org/10.1016/j.epsl.2012.05.014

Nara, Y., Meredith, P. G., Yoneda, T., & Kaneko, K. (2011). Influence of macro-fractures and micro-fractures on permeability and elastic wave velocities in basalt at elevated pressure. *Tectonophysics*, *503*, 52–59. https://doi.org/10.1016/j.tecto.2010.09.027

Neasham, J. W. (1977). The morphology of dispersed clay in sandstone reservoirs and its effect on sandstone shaliness, pore space and fluid flow properties.

Nemec, W. (1988). The shape of the rose. *Sedimentary Geology*, *59*, 149–152. https://doi.org/10.1016/0037-0738(88)90105-4

Norvick, M. S., & Smith, M. A. (2001). Mapping the plate tectonic reconstruction of southern and southeastern Australia and implications for petroleum systems. *Journal of the Australian Petroleum Production and Exploration Association*, *41*, 15–35.

Perincek, D., Simons, B., & Pettifer, G. R. (1994). The tectonic framework, and associated play types of the Western Otway Basin, Victoria, Australia. *APPEA Journal*, *34*, 460–477.

Pittman, E. D. (1979). Porosity, diagenesis and productive capacity of sandstone reservoirs. *SEPM Special Publication*, *26*, 159–173.

Rowland, J. V., & Sibson, R. H. (2004). Structural controls on hydrothermal flow in a segmented rift system, Taupo Volcanic Zone, New Zealand. *Geofluids*, *4*, 259–283. https://doi.org/10.1111/j.1468-8123.2004.00091.x

Schneider, C. L., Hill, K. C., & Hoffman, N. (2004). Compressional growth of the Minerva Anticline, Otway Basin, Southeast Australia–evidence of oblique rifting. *APPEA Journal*, *44*, 463–480.

Shipton, Z. K., & Cowie, P. A. (2001). Damage zone and slip-surface evolution over μm to km scales in high-porosity Navajo sandstone, Utah. *Journal of Structural Geology*, *23*, 1825–1844. https://doi.org/10.1016/S0191-8141(01)00035-9

Shipton, Z. K., Evans, J. P., Robeson, K. R., Forster, C. B., & Snelgrove, S. (2002). Structural heterogeneity and permeability in faulted eolian sandstone: Implications for subsurface modeling of faults. *AAPG Bulletin*, *86*, 863–883. https://doi.org/10.1306/61eedbc0-173e-11d7-8645000102c1865d

Sibson, R. H. (1994). Crustal stress, faulting and fluid flow. *Geological Society, London, Special Publications*, *78*, 69–84. https://doi.org/10.1144/gsl.sp.1994.078.01.07

Sibson, R. H., Moore, J. M. M., & Rankin, A. H. (1975). Seismic pumping—a hydrothermal fluid transport mechanism. *Journal of the Geological Society*, *131*, 653–659. https://doi.org/10.1144/gsjgs.131.6.0653

Streit, J. E., & Hillis, R. R. (2004). Estimating fault stability and sustainable fluid pressures for underground storage of CO2 in porous rock. *Energy*, *29*, 1445–1456. https://doi.org/10.1016/j.energy.2004.03.078

Tassone, D. R., Holford, S. P., Duddy, I. R., Green, P. F., & Hillis, R. R. (2014). Quantifying Cretaceous-Cenozoic exhumation in the Otway Basin, southeastern Australia, using sonic transit time data: Implications for conventional and unconventional hydrocarbon prospectivity. *AAPG Bulletin*, *98*, 67–117. https://doi.org/10.1306/04011312111

Tassone, D. R., Holford, S. P., Hillis, R. R., & Tuitt, A. K. (2012). Quantifying Neogene plate-boundary controlled uplift and deformation of the southern Australian margin. *Geological Society, London, Special Publications*, *367*, 91–110. https://doi.org/10.1144/sp367.7

Tassone, D. R., Holford, S. P., King, R., Tingay, M. R. P., & Hillis, R. R. (2017). Contemporary stress and neotectonics in the Otway Basin, southeastern Australia. *Geological Society, London, Special Publications*, *458*, https://doi.org/10.1144/sp458.10

Webb, P. A. (2001). *An introduction to the physical characterization of materials by mercury intrusion porosimetry with emphasis on reduction and presentation of experimental data*. Norcross, GA: Micromeritics Instrument Corp.

Wibberley, C. A. J., & Shimamoto, T. (2003). Internal structure and permeability of major strike-slip fault zones: The Median Tectonic Line in Mie Prefecture, Southwest Japan. *Journal of Structural Geology*, *25*, 59–78. https://doi.org/10.1016/S0191-8141(02)00014-7

Wilson, J. E., Chester, J. S., & Chester, F. M. (2003). Microfracture analysis of fault growth and wear processes, Punchbowl Fault, San Andreas system, California. *Journal of Structural Geology*, *25*, 1855–1873. https://doi.org/10.1016/S0191-8141(03)00036-1

Woodcock, N. H., Dickson, J. A. D., & Tarasewicz, J. P. T. (2007). Transient permeability and reseal hardening in fault zones: Evidence from dilation breccia textures. *Geological Society, London, Special Publications*, *270*, 43–53. https://doi.org/10.1144/gsl.Sp.2007.270.01.03

Zeng, L. (2010). Microfracturing in the Upper Triassic Sichuan Basin tight-gas sandstones: Tectonic, overpressure, and diagenetic origins. *AAPG Bulletin*, *94*, 1811–1825. https://doi.org/10.1306/06301009191

How to cite this article: Debenham N, Farrell NJC, Holford SP, King RC, Healy D. Spatial distribution of micrometre-scale porosity and permeability across the damage zone of a reverse-reactivated normal fault in a tight sandstone: Insights from the Otway Basin, SE Australia. *Basin Res*. 2019;31:640–658. https://doi.org/10.1111/bre.12345